CIMAC CONGRESS 25
ZURICH, MAY 19 – 23, 2025

2025 | 344

Rotordynamic performance prediction of electrically assisted turbocharger

Mechanics, Materials & Coatings

Baoyin Duan, Harbin Engineering University

Chuanlei Yang, Harbin Engineering University
Hechun Wang, Harbin Engineering University
Yinyan Wang, Harbin Engineering University
Hua Shen, Chongqing Jiangjin Shipbuilding Industry Co., Ltd
Yang Liu, Chongqing Jiangjin Shipbuilding Industry Co., Ltd

ABSTRACT

Electrically assisted turbocharging (EAT) technology is an important technical means to improve engine power response and achieve electrification of ship power systems. There is currently little research on the reliability of EAT rotors. Based on a physical rotor of marine turbocharger, this article established a corresponding finite element model and verified the model. Subsequently, the dynamic design of the EAT rotor was carried out, and analysis revealed that the EAT rotor exhibited unacceptable vibrations. Further research was conducted on the differences in linear and nonlinear results of EAT rotor system between three bearing forms: full floating ring bearings (FRB), semi-floating ring bearings (SFRB), and semi-floating ring bearings with three-oil wedge shapes inside the ring (3-lobed SFRB). The results indicate that the FRB-rotor system exhibits a wide range of 0.12X frequency vibrations, and its axis trajectory fluctuates greatly with the rotational speed. Although the ordinary SFRB-rotor system exhibits relative stability in the axis trajectory, there are three vibration components: 1X, 0.5X, and 0.12X, and the vibrations are quite severe. By comparing the simulation results, the operating speed range of the EAT rotor supported by 3-lobed SFRB is far from its critical speed and the level of sub-synchronous vibration is relatively low within this range. In addition, the rotor has appropriate unbalance effects. At this point, the EAT rotor integrated with the motor rotor exhibits better operational stability. This study can effectively assist in the design and analysis of EAT.

1 INTRODUCTION

With the rapid development of the global transportation industry, non-renewable fossil fuels are rapidly being consumed. Energy shortage, environmental pollution, greenhouse effect and other issues have attracted widespread attention[1-4]. Driven by energy conservation, emission reduction, and environmental protection policies, governments around the world have introduced a series of industrial policies to promote the development of the engine parts industry. After decades of commercial application, exhaust turbocharged engines have demonstrated their advantages[5-6]. After compression, air enters the engine, allowing more fuel to be injected into engines of the same size, improving the overall efficiency of the combustion process and thus increasing the engine's power and torque. Nowadays, exhaust gas turbochargers (TC) have become an indispensable part of modern internal combustion engines, and their application scenarios have expanded to multiple fields such as vehicles and ships[7].

Undoubtedly, using exhaust gas to drive the turbine to rotate and then drive the compressor to work greatly improves the overall efficiency of the engine by increasing the intake of air. Currently, to further improve the performance of turbocharged engines, various technological improvements have emerged. For example, sequential turbocharging technology[8-10], two-stage turbocharging technology[11-13], and variable geometry turbine/compressor turbocharging technology[14-16]. However, the improved turbocharged engine studied above exhibits an inevitable drawback. The intake air increase is limited at low engine speed, and the transient performance needs to be improved. This phenomenon is also known as turbo lag. The electrically assisted turbocharger (EAT) effectively solves this problem. Through EAT technology, the low-speed torque and transient response of turbocharged engines can be significantly improved[17].

In recent years, many studies have demonstrated the superiority of EAT in improving engine performance through simulation and experimentation. Wagino W[18] conducted in-depth research on the impact of electric turbochargers (ETC) on engine performance and emphasized the feasibility of their efficient recovery. Liu Y[19] conducted strategy optimization on the control of electric superchargers. The results showed that the proposed control strategy effectively increased intake pressure and achieved lower NOx emissions. Mazanec JM[20] connected an electric compressor in series with a turbocharger, and the research results showed that the engine's BSFC was reduced by 18%, demonstrating sufficient power performance. Martinez-Boggio S[21] evaluated the coupling mode between a electric compressor and a turbocharger based on one-dimensional numerical methods. Proposing the coupled electric assisted turbocharger is the optimal layout. Gamache C[22] added an electric compressor to the exterior of the turbocharger engine and found that adding eBoost shortened the transient response time by 55%. Benitez JM[23] proposed an energy recovery scheme for turbocharged engines, which couples a high-speed motor to the turbocharger shaft. The research results indicate that a recovery rate of 1%-3% has been achieved. Galindo J[24] evaluated the potential of three different exhaust gas recirculation management strategies. Engine testing has shown that the electric turbocharger ensures a balance between BSFC and torque response. Figari M[25] conducted a quantitative study on hybrid turbochargers based on a one-dimensional model of a large marine dual fuel four stroke engine. Proposing the use of hybrid turbochargers can improve efficiency and reduce emissions.

From the above research, it can be seen that the integration of the motor and turbocharger can significantly improve the problem of engine acceleration response lag. However, there is no doubt that such changes to the original shaft system will affect the dynamic behavior of the rotor system. Therefore, it is necessary to conduct research on the dynamic response characteristics of EAT rotors, explore their vibration response laws that vary with various factors, and ensure the stable operation of the rotor[26]. Kong X[27] considered that EAT may be affected by complex external factors and studied the impact of external excitation on the system. The research results revealed the operating rules of the EAT rotor system under strong impact. Lee W[28] established a model of an electrically driven compressor supported by foil bearings. The inherent modes of the system under compressor shell excitation were identified through linear and nonlinear dynamic studies. Hu M[29] proposed that controlling the unbalance and oil film clearance can suppress the high amplitude asynchronous vibration of EAT.

The current research on EAT systems is mostly focused on improving engine performance. Meanwhile, there is relatively little research on the dynamic stability of EAT rotor systems. Therefore, it is necessary to conduct vibration response analysis on the EAT rotor, study the dynamic response characteristics, and ensure the safe and stable operation of the EAT. As an important support for the rotor system, the structure and parameters of oil film bearings have a significant impact on the rotor. The design of EAT rotors may also involve changes in the form of bearings. The

influence of differences in bearing forms on the vibration characteristics of EAT rotors has not been reported yet. This paper takes a certain type of marine floating ring bearing (FRB)-TC rotor system as the research object and carries out EAT rotor design based on the experimentally verified TC rotor model. Considering the influence of differences in bearing forms, a new bearing modeling was conducted based on the original FRB, and the effects of FRB, semi-floating ring bearing (SFRB), and 3-lobed SFRB on the dynamic characteristics of the rotor were studied. The research results provide a theoretical basis and reference for the stability study of EAT rotor systems, which is beneficial for reducing a large amount of experimental costs.

2 FRB-TC ROTOR MODEL

2.1 Rotor model

Currently, FRB has been widely used in TC systems for vehicles and ships. The cross-sectional view of the FRB used in a certain type of marine turbocharger is shown in Figure 1. The inner and outer membranes of FRB can be regarded as a series connection of two fluid film bearings. Ω_1 and Ω_2 represent the rotational speeds of the journal and ring respectively. The inner oil film has two rotating surfaces, namely the journal and the ring, while the outer oil film only has one rotating surface, namely the ring. In some designs, an anti-rotation pin is added to prevent the rotation of the ring. At this time, the internal oil film only has one rotating surface, which is the journal. At this time, the outer oil film does not undergo circumferential flow, and this type of bearing is called a SFRB. It can also be seen as a series connection of a journal bearing and a squeeze film damper (SFD).

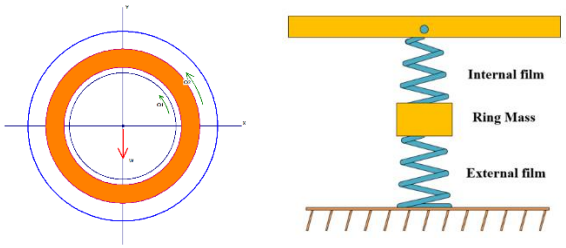

Figure 1. FRB model

The Reynolds equation for solving the dynamic pressure of the inner and outer oil film can be expressed as[30]:

$$\frac{1}{R_J^2}\frac{\partial}{\partial\alpha}\left(\frac{h_i^3}{12\mu_i}\frac{\partial P_i}{\partial\alpha}\right)+\frac{\partial}{\partial Z_i}\left(\frac{h_i^3}{12\mu_i}\frac{\partial P_i}{\partial Z_i}\right)=\frac{\Omega_1+\Omega_2}{2}\frac{\partial h_i}{\partial\alpha}+\frac{\partial h_i}{\partial t} \tag{1}$$

$$\frac{1}{R_o^2}\frac{\partial}{\partial\beta}\left(\frac{h_o^3}{12\mu_o}\frac{\partial P_o}{\partial\beta}\right)+\frac{\partial}{\partial Z_o}\left(\frac{h_o^3}{12\mu_o}\frac{\partial P_o}{\partial Z_o}\right)=\frac{\Omega_2}{2}\frac{\partial h_o}{\partial\beta}+\frac{\partial h_o}{\partial t} \tag{2}$$

where subscripts i and o are used to distinguish between internal and external oil film parameters. R_J and R_o correspond to the neck radius and ring outer radius respectively. α and β are the circumferential positions of the inner and outer oil films, respectively. P is the oil film pressure. h represents the oil film thickness. Z is the axial coordinate. μ is the lubricating oil viscosity.

The schematic diagram of the FRB reference frame is shown in Figure 2. Among them, O_b , O_r and O_J are the center of the bearing housing, the center of the ring, and the center of the journal, respectively. From the figure, it can be seen that the thickness of the inner and outer oil film can be expressed as:

$$h_i = C_i - x_i\cos\alpha - y_i\sin\alpha \tag{3}$$

$$h_o = C_o - x_r\cos\beta - y_r\sin\beta \tag{4}$$

Where C_i and C_o are the radial clearances between the inner and outer oil films, respectively. x_i and y_i are the displacements of the journal center relative to the center of the ring, which can be expressed as:

$$x_i = X_J - X_r \tag{5}$$

$$y_i = Y_J - Y_r \tag{6}$$

Where (X_J, Y_J) represents the displacement vector of the journal center in a fixed reference coordinate system. (X_r, Y_r) is the displacement vector corresponding to the center of the ring.

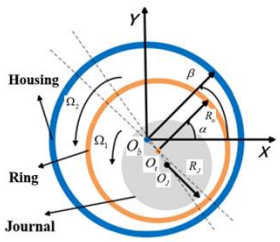

Figure 2. Schematic diagram of FRB coordinates

As the speed increases, the temperature of the lubricating oil filling the clearance will inevitably change. The viscosity curve of lubricating oil ISO-VG 100 as a function of temperature is shown in Figure 3. This figure can be obtained from the viscosity temperature equation and can be expressed as:

$$\mu = \mu_0 e^{-\lambda(T-T_0)} \tag{7}$$

Where T_0 represents the initial temperature. μ_0 corresponds to the viscosity.

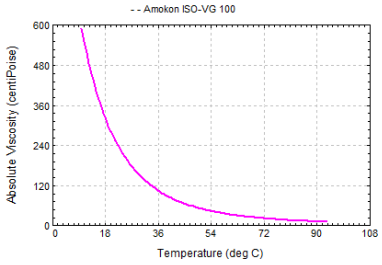

Figure 3. ISO-VG 100 viscosity-temperature curve

Solving for Eq. (1) and Eq. (2) based on the above analysis and obtaining the respective expressions for (P_i, P_o). Subsequently, the transient oil film pressure distribution (P_i, P_o) obtained by solving the Reynolds equation can be integrated to obtain the inner and outer film oil film forces:

$$\begin{bmatrix} F_{ix} \\ F_{iy} \end{bmatrix} = \sigma_i \left(\int_0^{L_i} \int_0^{2\pi} P_i \begin{bmatrix} \cos\alpha \\ \sin\alpha \end{bmatrix} R_i \, d\alpha \, dz \right) \tag{8}$$

$$\begin{bmatrix} F_{ox} \\ F_{oy} \end{bmatrix} = \sigma_o \left(\int_0^{L_o} \int_0^{2\pi} P_o \begin{bmatrix} \cos\beta \\ \sin\beta \end{bmatrix} R_o \, d\beta \, dz \right) \tag{9}$$

Where σ represents Sommerfeld coefficient. L_i and L_o are the effective lengths inside and outside the ring, respectively. The relevant structural parameters of the FRB are shown in Table 1. According to Table 1, the inner clearance C_i of the floating ring shaft supporting the rotor of this type of marine turbocharger is 0.12 mm, and the outer clearance C_o is 0.36 mm.

Table 1. FRB structural parameters

Name	Value
Journal diameter	24.499 mm
Floating ring inner diameter	24.739 mm
Floating ring outer diameter	35.732 mm
Internal effective length of ring	15.6 mm
External effective length of ring	20.2 mm
Bearing diameter	36.452 mm
Floating ring mass	0.0797 kg

Eq. (8) and Eq. (9) describe the nonlinear oil film forces of the inner and outer membranes, which can be embedded into the motion control equations of the rotor bearing system for conducting time transient analysis. The motion control equation of TC rotor-FRB system:

$$M\ddot{q}(t) + (C_b + \Omega G)\dot{q}(t) + Kq(t) = F_i + F_u + F_g \tag{10}$$

Where M, C_b, G, and K represent the mass matrix, bearing dynamic damping matrix, gyroscope matrix and stiffness matrix, respectively. $q(t)$ is the system displacement vector. F_g represents the gravity vector. The oil film force vector is shown in Eq. (8) and Eq. (9). The unbalanced force vector F_u exists at the end of compressor impeller and turbine, consisting of two parts, which can be represented as:

$$F_{uc} = \begin{Bmatrix} F_{uc}^x \\ F_{uc}^y \end{Bmatrix} = \begin{Bmatrix} m_c e\Omega^2 \cos(\Omega t + \varphi_c) \\ m_c e\Omega^2 \sin(\Omega t + \varphi_c) \end{Bmatrix} \tag{11}$$

$$F_{ut} = \begin{Bmatrix} F_{ut}^x \\ F_{ut}^y \end{Bmatrix} = \begin{Bmatrix} m_t e\Omega^2 \cos(\Omega t + \varphi_t) \\ m_t e\Omega^2 \sin(\Omega t + \varphi_t) \end{Bmatrix} \tag{12}$$

Where subscripts c and t represent the compressor and turbine, respectively. m_c and m_t respectively represent the weight of the impeller and turbine. φ is the initial phase angle of the unbalanced force.

Based on the basic structural parameters and dimensions of the TC rotor bearing system, perform dynamic modeling on the compressor impeller, shaft, and turbine structures. The dynamic finite element model of the TC rotor-bearing system was established as shown in Figure 4. The rotor is divided into 7 stations. Stations 2 and 6 respectively represent the center of gravity positions of the compressor impeller and turbine. Stations 4 and 5 represent the positions on the rotor shaft corresponding to the center of the floating ring bearing. The red mark near station 5 indicates the center of gravity position of the TC rotor. Stations 8 and 9 respectively represent the rings at the compressor end and turbine end, which are

considered as single degree of freedom mass blocks with a mass of 0.0797 kg.

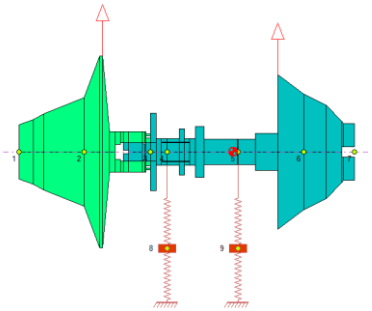

Figure 4. Rotor dynamics finite element model of FRB-TC

2.2 Model validation

The linearization of the bearing oil film coefficients is based on the assumption of small displacement perturbation, and the stiffness/damping coefficients are extracted through partial derivatives. Due to the high-speed characteristics of the turbocharger rotor, the internal and external oil film coefficients are preprocessed into segmented interpolation functions of speed and eccentricity to improve computational efficiency. The angular velocity of the floating ring is determined by the dynamic balance of the internal and external oil film shear moment and the floating ring inertia moment, and this coupling process is implicitly processed by a multi physics field solver. Although real-time weak coupling updates were not used, the parameterized scanning method has been experimentally validated for its effectiveness in predicting critical speeds. The first three critical speeds of the rotor obtained from the calculation are shown in Table 2.

Table 2. First three critical speeds of TC

	The first order	The second order	The third order
Speed (r/min)	7856	129874	275856

The acceleration velocity response curve generated by installing the TC rotor on the high-speed balancing machine is shown in Figure 5. The TC rotor exhibits two peaks in sequence, approximately at 8000 r/min and 125000 r/min, roughly corresponding to the first two critical speeds calculated by the rotor model. Due to factors such as rotor assembly, there may be some differences between experimental data and simulation results, but the error is within an acceptable range. Therefore, the accuracy of the finite element model of the FRB-TC rotor established has been verified.

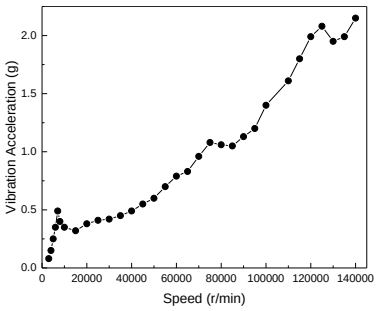

Figure 5. Response curve of TC rotor on high-speed balancing machine

3 EAT ROTOR DESIGN

At present, EAT mainly has coaxial and non-coaxial structural designs. The non-coaxial design involves adding an electrically driven compressor upstream or downstream of the TC. Coaxial design integrates the motor between the compressor impeller and turbine or on the intake side of the compressor. Two common coaxial EAT engine structural diagrams are shown in Figure 6.

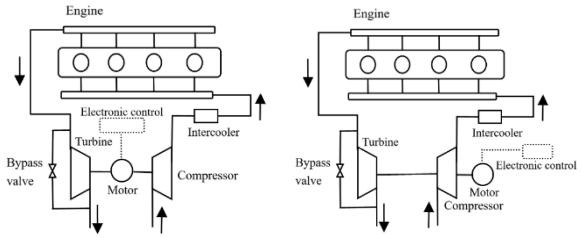

(a) Mid-mounted arrangement

(b) Front arrangement

Figure 6. Schematic diagram of coaxial EAT engine structure

From Figure 6 (a), the high temperature at the turbine end of the motor placement scheme will have a significant impact on the motor, such as demagnetization and other issues. In the current reported research, EAT studies mostly focus on mid-mounted motors. Meanwhile, these studies overlooked the impact of high temperatures on motors. By comparison, the front mounted motor can effectively avoid this situation. In addition, the current research on air gap motors has greatly reduced the impact on compressor intake. However, various forms of EAT are far from large-scale commercial applications and mostly exist in the laboratory stage. One of the important reasons to consider is their stability. Undoubtedly, the assembly of the motor has changed the balance of the original shaft system, which may exacerbate

the vibration. This study integrates the brushless DC motor rotor on the inlet side of the TC rotor compressor. Selected samarium cobalt permanent magnets and added a layer of titanium alloy protective cover on the outer side of the permanent magnets to further prevent them from falling off at high speeds. The structural parameters of the motor rotor are shown in Table 3.

Table 3. The structural parameters of motor rotor

Structure	Value (mm)
Inner diameter of permanent magnet	15
Outer diameter of permanent magnet	45
Inner diameter of permanent sleeve	45
Outer diameter of protective sleeve	20
Rotor length	107

The motor rotor is integrated on the inlet side of the compressor and coaxially connected with the compressor. The finite element model of the FRB-EAT rotor system is established as shown in Figure 7. The EAT rotor consists of 11 Stations. It is obvious that the center of gravity of the rotor moves from the support position near the turbine end bearing to the middle position of the two FRBs.

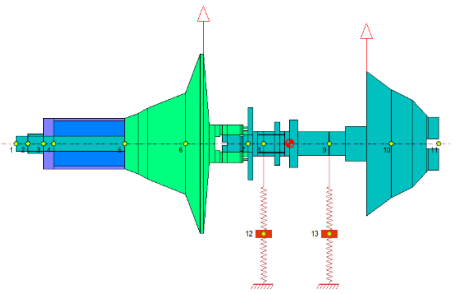

Figure 7. Finite element model of EAT

In the following vibration response of EAT rotors supported by FRB, SFRB, and 3-lobed SFRB, the main dimensions (journal diameter, bearing width, inner and outer length of the ring, etc.) and nominal oil film clearance (inner and outer oil film clearance) of all bearings are kept consistent. The difference is only reflected in the bearing structure and oil film boundary conditions. FRB： Independent lubrication of oil film, free rotation of floating ring; SFR： Outer membrane fixation, inner membrane free lubrication; 3-lobed SFRB: The floating ring is fixed, and the internal shape of the ring is designed as a three-oil wedge shape, with the outer film maintaining a circular bearing form.

4 RESULTS AND DISCUSSION

Predicting the stability of the designed EAT rotor is crucial. Different forms of bearings will inevitably lead to significant differences in the dynamic behavior and evolution of EAT rotors. The rotor dynamics analysis based on linearized bearing dynamic coefficients can predict the critical speed and modal vibration mode of EAT rotors to a certain extent. At the same time, it also provides a path for predicting the 1X frequency vibration response of the rotor. However, the EAT rotor system supported by oil film bearings exhibits significant nonlinearity, and the actual motion of the rotor will show responses at other frequencies. Linear analysis cannot predict the severity of vibrations at other frequencies.

Therefore, this chapter focuses on the EAT rotor system and conducts linear and nonlinear analysis of the rotor with different bearing forms and speeds as variables. Firstly, the critical speed position was considered based on the actual operating speed range of EAT. Subsequently, time transient analysis was conducted to study the axial trajectory of the rotor at a specific speed under different bearing forms, and to analyze the vibration response at various frequencies. Finally, based on the above analysis, a comparative discussion was conducted.

4.1 Critical speed and mode analysis

During the EAT acceleration process, resonance occurs when the frequency of external excitation is equal to the natural frequency of the rotor, resulting in a sharp increase in amplitude. This phenomenon may cause bearing wear and even failure, posing a threat to the structure and performance of EAT rotors. Determine the resonance frequency and mode of vibration through critical speed and modal analysis. Study whether the rotor will operate at resonance position and whether vibration faults will occur during operation. Comparing three types of bearing forms through this analysis is helpful in understanding the dynamic characteristics of the rotor. Therefore, determining its critical speed and stability, which is crucial for the selection of bearing forms for the rotor.

To make linearization closer to the actual situation, the bearing module of professional software is used to model and calculate the bearing. Export the obtained stiffness and damping coefficients as the basic parameters for rotor modeling. Perform critical speed and mode analysis on the rotors supported by the three types of bearings established. The first four critical speeds and modes are shown in Figure 8. The corresponding critical speed are shown in Table 3.

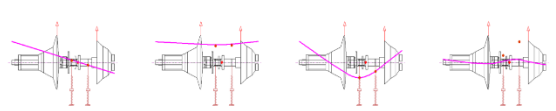

(a) FRBs

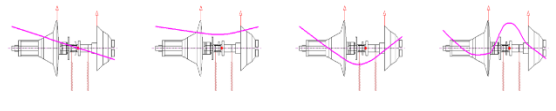

(b) SFRBs

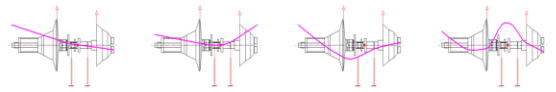

(c) 3-lobed SFRBs

Figure 8. First four modal shapes with different bearing forms

As shown in Figure 8:

(a) Under different bearing forms, the first three modal shapes of the rotor are similar. The first stage is the rigid cone mode, where the impeller and turbine move out of phase. The second order is the rigid cylindrical mode and the third order is the bending mode.

(b) At the fourth critical speed position, it can be seen that the two SFRBs also have similar modal shapes.

According to Table 4:

(a) The difference in bearing form will have a significant impact on the magnitude of the critical speeds at each order.

(b) The rotors supported by FRBs and SFRBs have a critical speed within the operating speed range, which is not conducive to the stable operation of the rotor. The second and third critical speed positions of the 3-lobed SFRB rotor effectively avoid the operating speed range.

According to the magnitude of the critical speeds and the mode shapes, there is no resonance phenomenon in the operating speed range of the EAT rotor with 3-lobed SFRB. That is to say, the rotor far avoids the resonance position in the operating speed range. Therefore, from the perspective of linearization analysis, the rotor supported by a 3-lobed SFRB will not experience strong vibration, and the rotor system will operate stably.

Table 4. First four critical speeds of EAT rotor under different bearing forms (unit: r/min)

	First order	Second order	Third order	fourth order
FRB	1299	4535	40301	153098
SFRB	2234	7402	44735	234656
3-lobed SFRB	8840	16641	83038	266532

4.2 Time Transient Analysis

Due to the fact that the EAT rotor is supported by oil film bearings, its axis trajectory will change with the variation of rotational speed. By describing the axis trajectory at specific speeds, the variation of oil film force can be effectively analyzed. At the same time, the waterfall plot and corresponding response spectral density plot show the variation of the EAT rotor vibration signal with frequency and time. Through this analysis, the synchronous/sub-synchronous vibration characteristics of the EAT rotor system can be understood.

The vibration response and evolution of EAT rotors under the coupling effects of oil film force, unbalanced force, and gravity are extremely complex. To predict the complete motion, this section conducted time transient analysis on EAT rotors with different bearing forms. The solution method adopts the Newmark-β integration method. The rotor node position studied is the endpoint Station 1.

4.2.1 FRB-EAT rotor

To explain the vibration pattern of the FRB-EAT rotor as the speed changes, Figure 9 depicts the changes in the axis trajectory of the rotor at 10000 r/min-100000 r/min. The unit of the images coordinate axis are mm. From Figure 9, it can be seen that:

(a) At a low speed of 10000 r/min, there is a significant displacement of the rotor axis. The axis moved to the lower right position, reaching a balanced position. The journal whirls around the equilibrium position and exhibits linear characteristics. The reason is that at low speeds, the distribution of oil film force may be uneven, and the rotor is also affected by gravity. This phenomenon occurs under the coupling effect of oil film force and gravity.

(b) As the rotational speed increases, this offset phenomenon disappears. The rotor trajectory moved upward, gradually forming a closed bounded limit cycle (BLC).

(c) As the speed further increases, the oil film force provides more significant support to the rotor, and the axis trajectory becomes more stable and regular. The axis trajectory is close to a circle, indicating that the operating state of the rotor is stable.

(d) Meanwhile, it can also be observed from the images that the trajectory radius of the rotor gradually increases with the increase of rotational speed. At this point, it is necessary to be cautious as rotor-stator friction may occur.

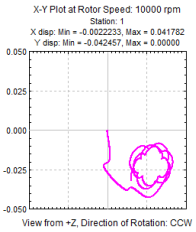

（a）10000 r/min

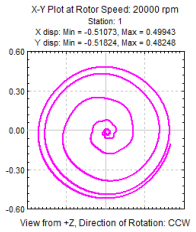

（b）20000 r/min

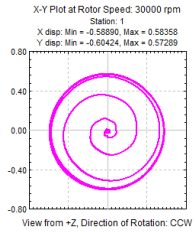

（c）30000 r/min

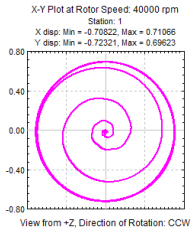

（d）40000 r/min

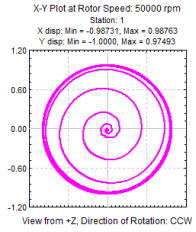

（e）50000 r/min

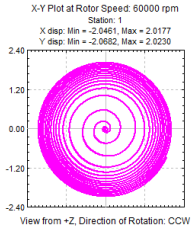

（f）60000 r/min

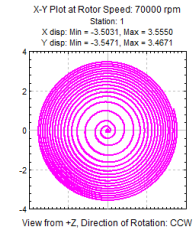

（g）70000 r/min

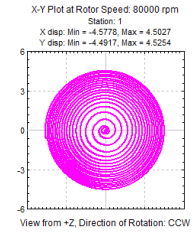

（h）80000 r/min

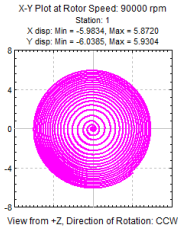

（i）90000 r/min

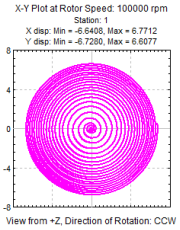

（j）100000 r/min

Figure 9. Changes in the axis trajectory of FRB-EAT rotor

Figure 10 shows the vibration response waterfall plot and corresponding response spectral density plot of the FRB-EAT rotor. In the response spectral density plot, colors represent the magnitude of amplitude, corresponding to an increase in response amplitude: yellow, light blue, dark blue, and red. From Figure 10, it can be seen that:

(a) The FRB-EAT rotor shows almost no frequency doubling or division vibration within the speed range from the simulated calculation speed to 15000 r/min.

(b) At around 15000 r/min, a vibration component of 0.12X frequency begins to appear in the rotor. The vibration component subsequently persisted throughout the entire acceleration range, which dominating the vibration of the rotor.

(c) It should be noted that the amplitude of this 0.12X vibration further increases at 55000 r/min. This sub-synchronous vibration is caused by oil film whirl/whip. In current reports, high amplitude sub-synchronous vibrations are associated with unacceptable noise generated by the rotor.

(d) After 80000 r/min, the system experienced oil film whip, making it difficult for the rotor to operate stably.

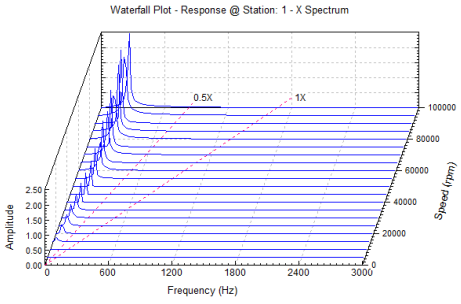

(a) Waterfall Plot

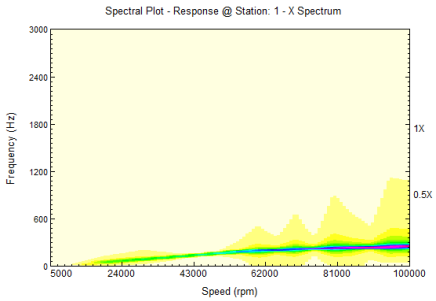

(b) Response spectral density plot

Figure 10. Rotor vibration response diagram of FRB-EAT

4.2.2 SFRB-EAT rotor

For FRBs of the same type as the previous section, an additional pin is used to prevent the rotation of the ring. At this point, the ring can only translate in a small range and cannot rotate. The external oil film will not undergo circumferential flow, which can be regarded as an SFD. Figure 11 shows the axial trajectory of a typical SFRB-EAT rotor at specific speeds. It can be clearly seen that there is a difference in the trajectory of the FRB-EAT rotor. Its characteristics are as follows:

(a) At low speeds, the axis trajectory of the rotor system exhibits stable single cycle motion. Due to the more significant influence of gravity, the axis trajectory moves downward with almost no deflection.

(b) As the rotational speed increases, the shape of the axis trajectory changes. The rotor trajectory exhibits a BLC between 50000 r/min and 80000 r/min. This indicates that the system has entered an oil film whirl state. The system may experience oil film instability accompanied by sub-synchronous vibration.

(c) At high speeds, the axis trajectory of the rotor becomes more complex, and the BLC is no longer apparent. The trajectory presents a solid circular shape. As the speed further increases, the system may enter an oil film oscillation state.

(d) Analyzing the radius of the rotor axis trajectory, it can be found that the size of the trajectory radius first increases, then decreases, and then increases again. This is related to the low-speed instability, medium-speed stability, and high-speed instability of the oil film.

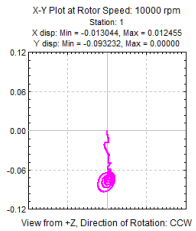

（a）10000 r/min

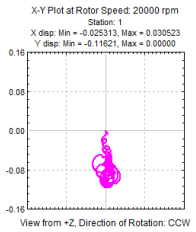

（b）20000 r/min

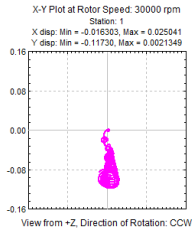

（c）30000 r/min

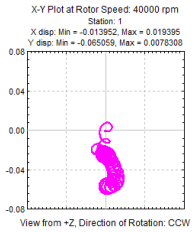

（d）40000 r/min

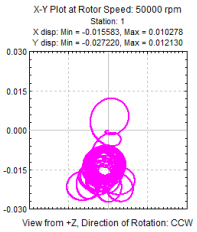

（e）50000 r/min

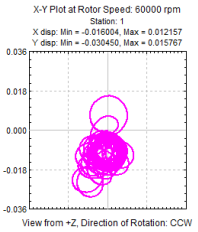

（f）60000 r/min

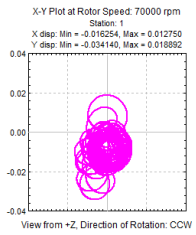

（g）70000 r/min

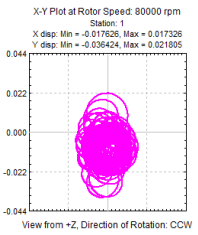

（h）80000 r/min

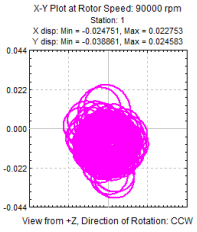

（i）90000 r/min

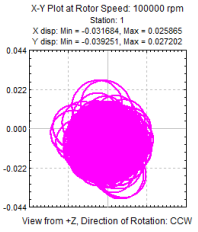

（j）100000 r/min

Figure 11. Changes in the axis trajectory of normal SFRB-EAT rotor

Figure 12 shows the waterfall plot and corresponding response spectral density plot of the vibration response of a normal SFRB-EAT rotor. The general conclusions of the obtained results are as follows:

(a) In the figure, three vibration frequency components can be observed, mainly including 1X frequency, 0.5X frequency and 0.12X frequency. In addition, a 0 Hz "DC" phenomenon occurred at low speeds.

(b) At the initial stage of the acceleration process, up to 43000 r/min, the vibration of the system is mainly dominated by 1X frequency and 0.5X frequency. At 43000 r/min to 77000 r/min, the rotor vibration is dominated by 1X frequency vibration, indicating good system stability. When the speed exceeds 77000 r/min, 0.12X frequency vibration occurs with 1X frequency, and the two dominate the rotor vibration.

(c) At low speeds, the 0.5X frequency amplitude is relatively high and the vibration is more intense. This is due to the oil film not filling the clearance occurring in the low-speed range (<43000 r/min). The reason is that the fixed design of the outer oil film limits the oil supply capacity at low speeds, resulting in partial filling phenomenon, which in turn causes local lubrication film instability.

(d) Within the speed range of EAT operation, it can be observed that the rotor exhibits intermittent instability at 30000 r/min-43000 r/min due to the sudden intensification of oil film whirl at 0.5X frequency. Therefore, it is necessary to pay more attention to the rotor state at this position to prevent unforeseen system failures.

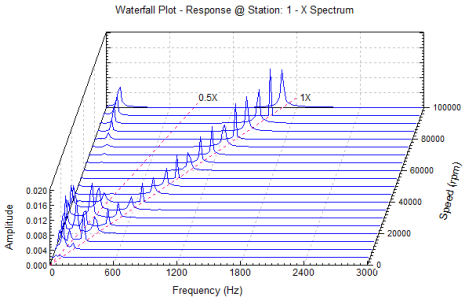

(a) Waterfall Plot

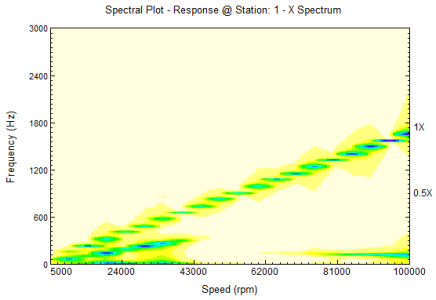

(b) Response spectral density plot

Figure 12. Rotor vibration response diagram of normal SFRB-EAT

Additionally, there is a 0.5X frequency vibration component in the vibration response. The root cause of its appearance is mainly due to the nonlinear dynamic effects of internal oil film shear flow. The first is the excitation of oil film whirl: the high-speed shear flow of the inner oil film forms a circumferential pressure gradient when the rotor is eccentric, inducing a whirling motion of the rotor. When the whirl frequency approaches the natural frequency of the system, it will cause sub-synchronous resonance. The second is inertial detuning. After the outer oil film is fixed, the inertia effect of the ring is partially suppressed, but its remaining degrees of freedom still cause decoupling between the whirl frequency of the inner oil film and the damping response of the outer oil film. This decoupling effect causes the whirl frequency to be about half of the shaft frequency, resulting in 0.5X frequency vibrations.

4.2.3 3-lobed SFRB-EAT rotor

Based on the dimensions of the SFRB structure in the previous section, the internal shape of the ring is designed as a three-oil wedge shape, called 3-lobed SRFB. Observe the vibration response of the EAT rotor system. The results of the axis trajectory at specific speeds are shown in Figure 13. The results indicate that:

(a) At lower speeds, due to gravity, the axis of the rotor exhibits linear characteristics and the trajectory moves downwards. At this time, the dynamic pressure effect of the oil film has not been fully exerted, so the offset is relatively small.

(b) As the speed increases, the dynamic pressure effect of the oil film gradually strengthens, and the axis trajectory of the rotor shows significant changes. At this point, the axis trajectory is relatively complex.

(c) At high speeds, the rotor operates on a BLC. However, it should be noted that the oscillation caused by unstable oil film may make the rotor more unstable, and even lead to chaotic phenomena.

(d) From the figure, it can be seen that the three-oil wedge type bearing is more conducive to the support of the oil film on the rotor. In addition, the good damping effect of the external oil film also maintains the stability of the rotor axis trajectory. Therefore, the radius of the axis trajectory shows a decreasing-increasing-stable state.

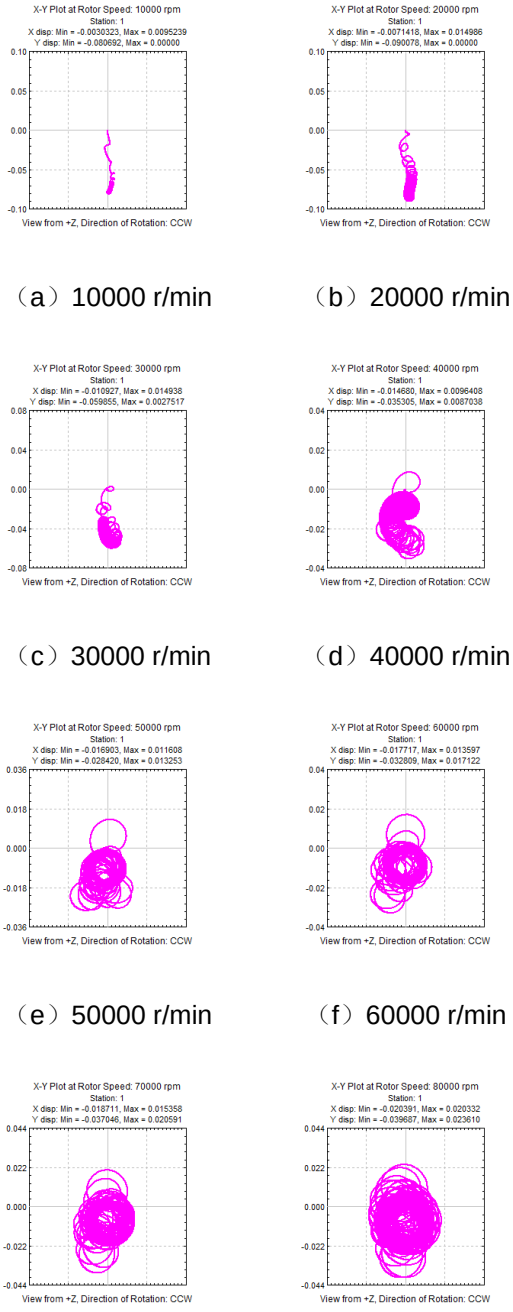

（a）10000 r/min （b）20000 r/min

（c）30000 r/min （d）40000 r/min

（e）50000 r/min （f）60000 r/min

（g）70000 r/min （h）80000 r/min

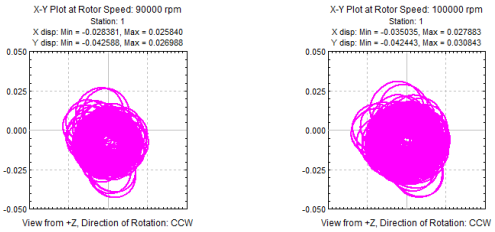

（i）90000 r/min （j）100000 r/min

Figure 13. Changes in the axis trajectory of 3-lobed SFRB-EAT rotor

Figure 14 shows the 3D vibration waterfall plot of 3-lobed SFRB-EAT and its corresponding response spectral density plot. From the figures, it can be seen that:

(a) The 1X frequency persists throughout the entire calculation range. However, this type of vibration is strengthened at 16000 r/min. This is because this position is related to the critical speed, corresponding to section 3.1. This also demonstrates the effectiveness of linear analysis in predicting synchronous vibrations.

(b) After 50000 r/min, the 1X frequency enhances. The reason is that the rotor is subjected to various forces such as centrifugal force, gyroscopic moment, and unbalanced force during high-speed rotation. In addition, this is also related to poor lubrication of the bearing and insufficient support stiffness. Attention should be paid to the severe vibration that occurs during continuous high-speed operation, which can accelerate bearing wear and reduce service life.

(c) Starting from 77000 r/min, 0.12X synchronous vibrations begin to appear and gradually increase at high speeds.

(d) Within the operating speed range of the EAT rotor, there are no 0.5X and 0.12X components. The 1X frequency vibration will intensify at the upper limit of this range. Indicating that 3-lobed SFRB can absorb and dissipate vibration energy, reducing the overall vibration of the system. It should be noted that the performance of the damper will be affected at high speeds.

(e) Due to the optimization of the internal geometry of the 3-lobed SFRB through pre-set pressure gradients and shear rates, continuous oil film coverage is ensured throughout the entire

speed range, thereby suppressing partially filled nonlinear vibrations (0.5X).

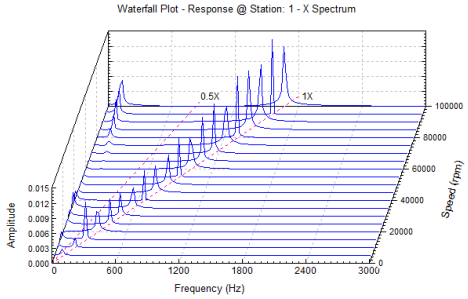

(a) Waterfall Plot

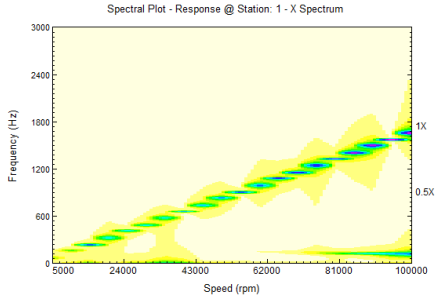

(b) Response spectral density plot

Figure 14. Rotor vibration response diagram of 3-lobed SFRB-EAT

4.3 Comparative Analysis

The bearing-EAT rotor model established based on linearized bearing dynamic characteristic coefficients shows that the critical speed of the 3-lobed SFRB-EAT rotor far avoids the EAT operating speed range of 30000 r/min-60000 r/min. Therefore, compared with FRB and normal SFRB, the 3-lobed design of SFRB is a better choice in linear sense.

To compare the differences in the trajectory size of the EAT rotor axis supported by different bearing forms more clearly, Figure 15 shows the radius size of the trajectory in the Y direction (vertical direction) at the station 1. Using rotational constraints on the ring can significantly reduce self-excited vibration. The trajectory radius of the rotor is greatly reduced at a specific speed, effectively reducing the overall amplitude of the rotor.

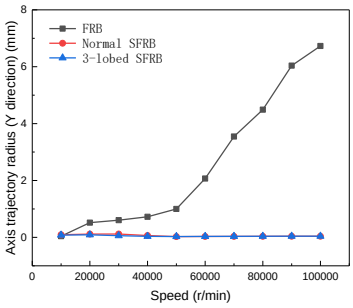

Figure 15. The variation of axis trajectory radius with rotational speed

However, the difference between normal SFRB and 3-lobed SFRB in terms of axis trajectory radius is not significant. Therefore, it is necessary to further compare the vibration response of rotors. Table 5 summarizes the vibration conditions of different bearing forms (1X, 0.5X, and 0.12X). According to the data analysis in Table 5, the FRB-EAT rotor exhibits high amplitude 0.12X vibration at 15000 r/min-10000 r/min. The normal SFRB-EAT rotor exhibits a more complex vibration response, with 1X, 0.5X, and 0.12X vibrations occurring simultaneously or alternately. High amplitude sub-synchronous vibration can easily disrupt the stability of the rotor, leading to abnormal displacement or fluctuations in the rotor. Excessive 1X vibration will exacerbate the unbalance effect, generating greater centrifugal force during rotor acceleration, thereby increasing the load and wear of the rotor.

By comparing the rotor vibration of three types of bearings, the 3-lobed SFRB exhibits appropriate unbalance effects. The content of sub-synchronous vibration is relatively low, and the vibration is suppressed, working in a relatively stable state within the operating speed range. Meanwhile, there are also reports suggesting that using 3-lobed bearings with dampers can effectively reduce bearing oil temperature. Therefore, the proposed 3-lobed SFRB design can effectively improve the dynamic characteristics of EAT rotors and enhance their operational stability.

Table 5. Vibration frequency ranges of rotors with different bearing forms (unit: r/min)

	FRB	Normal SFRB	3-lobed SFRB
1X	-	5000-100000	5000-100000
0.5X	-	5000-43000	-
0.12X	15000-100000	77000-	77000-

Through this study, the 3-lobed SFRB has a significant improvement effect on the vibration response of the designed EAT rotor. In the

following work, the influence of structural parameter changes of 3-lobed bearings on the dynamic characteristics of EAT rotors will be considered. Study its evolution law and find a more reasonable range of design parameters. Furthermore, manufacture a prototype of the EAT rotor, build a test bench, and conduct experimental verification. Additionally, the gained experience can be applied to the design of other types of rotor-bearing systems.

5 CONCLUSIONS

EAT is of great significance in improving the operational efficiency and addressing complex operating challenges. Firstly, a finite element model of a certain type of marine TC rotor was established and validated. Subsequently, integrate the motor rotor onto the compressor impeller side. Finally, considering the impact of support on the EAT rotor, the bearings were designed based on the TC prototype FRBs, taking into account three different bearing forms: FRB, normal SFRB, and 3-lobed SFRB. The dynamic stability of the EAT rotor was studied through numerical calculations. The conclusions are as follows:

1. The EAT rotors with three different support forms have similar first three modal shapes. However, the rotors of FRB and normal SFRB have critical speeds within the EAT operating speed range, which is not conducive to stable operation. In contrast, the 3-lobed SFRB, through its special design, not only exhibits good vibration modes, but also the critical speed position is far away from its operating speed.

2. The trajectory of FRB-rotor system fluctuates greatly with the speed. Thanks to the excellent lubrication performance and damping effect of SFRB bearings, the axis trajectory of the rotor supported by SFRB and 3-lobed SFRB is relatively stable. The rotor can also maintain a small amplitude and offset at high speeds.

3. The EAT rotor supported by FRB exhibits a large range of 0.12X frequency components. There is no 1X frequency and no obvious resonance characteristics. The EAT rotor supported by normal SFRB has three types of vibration components, which are complex and exhibit oil film whirl instability at low speeds. The 3-lobed SFRB, due to its excellent damping effect and vibration suppression capability, significantly reduces the vibration noise level of the rotor during operation and can maintain good vibration noise performance.

4. The research conclusions provide important theoretical basis and data support for the design and optimization of EAT, which is of great significance for improving the performance stability and reliability of EAT. In future research, more advanced bearing forms and improvement measures will continue to be explored to further enhance the overall performance of EAT-engines.

6 DEFINITIONS, ACRONYMS, ABBREVIATIONS

English letters

C	Damping matrix
e	Unbalanced eccentricity
F_u	Unbalanced force
F_g	Gravity
F_i	Nonlinear oil film force
G	Gyroscopic matrix
G_x / G_z	Turbulence coefficients
h	Oil film thickness
K	Stiffness matrix
L	Floating effective length
M	Mass matrix
m_c / m_t	Compressor impeller/turbine weight
O_b	Bearing housing center
O_j	Journal center
O_r	Ring center
P	Oil film pressure

R_J	Journal radius
R_o	Floating outer radius
Z	Axial coordinate along the rotor center

Greek letters

α / β	Angle along the shaft rotation direction
μ	Oil film viscosity
φ	Initial angle applied unbalanced force
Ω	Rotor speed

Abbreviations

BLC	Bounded limit cycle
EAT	Electrically assisted turbocharger
FRB	Floating ring bearing
SFRB	Semi-floating Ring Bearing
SFD	Squeeze film damper
TC	Turbocharger

7 REFERENCES

[1] Mazuro P, Kozak D. 2024. Effect of variable geometry turbocharger on the performance of the opposed piston engine–An experimental approach, Applied Thermal Engineering, 236: 121602.

[2] Chen S, Ma C, Zhang H, et al. 2022. Engine performance improvements through turbocharger matching and turbine design, Energy Science & Engineering, 10(9): 3384-3396.

[3] Zhou F, Meng Z, Xiao X, et al. 2024. Pre-matching study of the natural gas engine turbocharging system based on the coupling of experiments and numerical simulation, Mechanics & Industry, 25: 2.

[4] Hu S, Wang H, Niu X, et al. 2018. Automatic calibration algorithm of 0-D combustion model applied to DICI diesel engine, Applied Thermal Engineering, , 130: 331-342.

[5] Park C, Ebisu M, Bae C. 2021. Effects of turbocharger rotation inertia on instantaneous turbine efficiency in a Turbocharged-Gasoline Direct Injection (T-GDI) engine, Journal of Engineering for Gas Turbines and Power, 143(1): 011006.

[6] Nyongesa A J, Park M H, Lee C M, et al. 2024. Experimental evaluation of the significance of scheduled turbocharger reconditioning on marine diesel engine efficiency and exhaust gas emissions, Ain Shams Engineering Journal, 102845.

[7] Prévost F, Le Moual Y, Maiboom A, et al. 2023. An analytical user-friendly methodology to transform compressor and turbine supplier characterization maps dedicated to 1D engine simulation: Modelling of turbocharger heat transfer and friction losses, Applied Thermal Engineering, 221: 119812.

[8] Shi M, Wang H, Yang C, et al. 2022. Experimental Research on the Matching Characteristics of the Compound VGT-STC System with a V-Type Diesel Engine, Machines, 10(9): 788.

[9] Li Y, Shi F. 2024. Discussion on the application of sequential turbocharging technology on trawlers, Proceedings of the Institution of Mechanical Engineers, Part E: Journal of Process Mechanical Engineering, 09544089241251633.

[10] Jia J, Zhu S, Zhou X, et al. 2024. Research on thermal-structural coupling and structural optimization of switching valve in booster system, Proceedings of the Institution of Mechanical Engineers, Part C: Journal of Mechanical Engineering Science, 238(6): 1911-1931.

[11] Lu Z, Yang M, Liu Y, et al. 2024. Unsteady aerodynamic interaction in regulated two-stage radial turbine at pulsating conditions, International Journal of Heat and Fluid Flow, 110: 109563.

[12] Zhang Y, Zhang F, Leng L, et al. 2023. Matching and optimization to minimize fuel consumption and NOx emission for a marine diesel engine with turbo-assisted exhaust gas recirculation, Proceedings of the Institution of Mechanical Engineers, Part D: Journal of Automobile Engineering, 09544070231210904.

[13] Peng Q, Zhang Z, Zhou G, et al. 2023. Experimental Study on the Flow Characteristics of Two-Stage Variable Turbines in a Twin-VGT System, Energies, 16(23): 7873.

[14] Zhang S, Sun B, Gui Y, et al. 2024. Experimental optimization of the performance and energy distribution of a direct injection hydrogen engine with analysis of application to onboard hydrogen storage methods, Sustainable Energy Technologies and Assessments, 72: 104034.

[15] Ma T, Li C, Xu Z, et al. 2024. Modeling and simulation of the PEMFC system equipped with a variable geometry turbocharger, International Journal of Hydrogen Energy, 77: 1327-1338.

[16] Mazuro P, Kozak D. 2024. Effect of variable geometry turbocharger on the performance of the opposed piston engine–An experimental approach, Applied Thermal Engineering, 236: 121602.

[17] Gamache C, Van Nieuwstadt M, Martz J, et al. 2024. LQTI boost pressure and EGR rate control of a diesel air charge system with eBoost assistance, International Journal of Engine Research, 14680874241241364.

[18] Wagino W, Fernandez D, Alwi E, et al. 2024. Exhaust Gas Flow Study of Electric Turbo Compounding (ETC) to Determine the Potential Electrical Energy Recovery from Exhaust Emission[J]. TEM Journal, 13(3).

[19] Liu Y, Song Y, Leng L, et al. 2024. Effects of control strategies of the electric supercharger on transient processes of a turbocharged diesel engine, Energy, 307: 132427.

[20] Mazanec J M, Vang N S, Kokjohn S L. 2023. Enabling off-highway diesel engine downsizing and performance improvement using electrically assisted turbocharging, International Journal of Engine Research, 24(9): 4104-4126.

[21] Martinez-Boggio S, Di Blasio D, Fletcher T, et al. 2023. Optimization of the air loop system in a hydrogen fuel cell for vehicle application, Energy Conversion and Management, 283: 116911.

[22] Gamache C, Van Nieuwstadt M, Martz J, et al. 2023. Dual-output PID transient control of an electric-assisted air charge system, International Journal of Engine Research, 24(8): 3519-3531.

[23] Benitez J M, Alvarez-Icaza L, Becerra-Nunez G, et al. 2023. Energy Recovered in Exhaust Gases on Diesel Engine, Oriented to a Hybrid Drivetrain, IEEE Access, 11: 102926-102934.

[24] Galindo J, Climent H, De la Morena J, et al. 2023. Assessment of air management strategies to improve the transient response of advanced gasoline engines operating under high EGR conditions, Energy, 262: 125586.

[25] Figari M, Theotokatos G, Coraddu A, et al. 2022. Parametric investigation and optimal selection of the hybrid turbocharger system for a large marine four-stroke dual-fuel engine, Applied Thermal Engineering, 208: 117991.

[26] Duan B, Yang C, Shen H, et al. 2024. Influence of External Clearance Variation on Vibration Characteristics of Ship Electrically Assisted Turbocharger Rotor Bearing System, International Journal of Structural Stability and Dynamics, 2650035.

[27] Kong X, Guo H, Cheng Z, et al. 2024. Dynamic Characteristics of Electrically Assisted Turbocharger Rotor System Under Strong Impacts, Journal of Vibration Engineering & Technologies, 1-13.

[28] Lee W, Kim D. 2024. Rotordynamics of a rotor supported by foil bearings under various housing excitation, Tribology International, 199: 109956.

[29] Hu M, Cao S, Cao X, et al. 2024. Dynamics and stability analysis of unbalance responses in mid-positioned electrically assisted turbocharger rotor, International Journal of Mechanical System Dynamics.

[30] Ouyang X, Guo H, Wu X, et al. 2022. Investigation of weight effects on the critical speed of inclined turbocharger rotor system, Journal of Nonlinear Mathematical Physics, 29(2): 403-422.